Article

Nodeless electron pairing in CsV_3Sb_5-derived kagome superconductors

https://doi.org/10.1038/s41586-023-05907-x

Received: 19 July 2022

Accepted: 1 March 2023

Published online: 26 April 2023

Check for updates

Yigui Zhong[1,14], Jinjin Liu[2,3,14], Xianxin Wu[4,14], Zurab Guguchia[5], J.-X. Yin[6,7], Akifumi Mine[1], Yongkai Li[2,3,8], Sahand Najafzadeh[1], Debarchan Das[5], Charles Mielke III[5], Rustem Khasanov[5], Hubertus Luetkens[5], Takeshi Suzuki[1], Kecheng Liu[1], Xinloong Han[9], Takeshi Kondo[1,10], Jiangping Hu[11], Shik Shin[1,12,15], Zhiwei Wang[2,3,8]✉, Xun Shi[2,3]✉, Yugui Yao[2,3,8] & Kozo Okazaki[1,10,13]✉

The newly discovered kagome superconductors represent a promising platform for investigating the interplay between band topology, electronic order and lattice geometry[1–9]. Despite extensive research efforts on this system, the nature of the superconducting ground state remains elusive[10–17]. In particular, consensus on the electron pairing symmetry has not been achieved so far[18–20], in part owing to the lack of a momentum-resolved measurement of the superconducting gap structure. Here we report the direct observation of a nodeless, nearly isotropic and orbital-independent superconducting gap in the momentum space of two exemplary CsV_3Sb_5-derived kagome superconductors—$Cs(V_{0.93}Nb_{0.07})_3Sb_5$ and $Cs(V_{0.86}Ta_{0.14})_3Sb_5$—using ultrahigh-resolution and low-temperature angle-resolved photoemission spectroscopy. Remarkably, such a gap structure is robust to the appearance or absence of charge order in the normal state, tuned by isovalent Nb/Ta substitutions of V. Our comprehensive characterizations of the superconducting gap provide indispensable information on the electron pairing symmetry of kagome superconductors, and advance our understanding of the superconductivity and intertwined electronic orders in quantum materials.

Superconductivity often emerges in the vicinity of other ordered electronic states with a broken symmetry, such as antiferromagnetic order and charge density wave. Their interdependence has been widely studied in cuprate and iron-based superconductors[21,22], but persists as a key issue for understanding high-temperature superconductivity. In certain cases, the ordered state and superconductivity can even coexist[23], which may indicate an unconventional pairing and have a dramatic impact on the superconducting mechanism. Because of the unique lattice geometry and unusual electronic features in a kagome lattice[1,3,4], the recently discovered kagome superconductors stand out as a new platform for inspecting the superconductivity emerging from a complex landscape of electronic orders[5,7,24]. Of particular interest is the non-magnetic family of AV_3Sb_5 (A = K, Rb, Cs)[5,24], in which a variety of intriguing phenomena have been uncovered, including a tantalizing time-reversal symmetry-breaking charge density wave (CDW) order[9,25,26], a pair density wave[10], electronic nematicity[8,27,28], double superconducting domes under pressure[29,30] and giant anomalous Hall effect[31,32]. All these phenomena point out exotic intertwined effects in kagome superconductors AV_3Sb_5.

To illuminate the microscopic pairing mechanism and the cooperation/competition between multiple phases in such kagome superconductors, a fundamental issue is to determine the superconducting (SC) gap symmetry. This prominent issue remains elusive owing to the great challenge in resolving such small energy scales and the existence of several conflicting experimental results. Taking CsV_3Sb_5 as an example, certain V-shaped gaps, as well as residual Fermi-level states measured by scanning tunnelling spectroscopy[10,11] and a finite residual thermal conductivity towards zero temperature[12], seem to support a nodal SC gap. By contrast, the observations of the Hebel–Slichter coherence peak in the spin-lattice relaxation rate from $^{121/123}$Sb nuclear quadrupole resonance measurements[13] and the exponentially temperature-dependent magnetic penetration depth[14,15], are more consistent with a nodeless superconductivity. On the theoretical side, both unconventional and conventional superconducting pairing were proposed[18–20]. Therefore, an unambiguous characterization of the SC gap structure and its connection with the intertwined CDW order becomes an urgent necessity. During the long-term research of superconductors, angle-resolved

[1]Institute for Solid States Physics, The University of Tokyo, Kashiwa, Japan. [2]Centre for Quantum Physics, Key Laboratory of Advanced Optoelectronic Quantum Architecture and Measurement (MOE), School of Physics, Beijing Institute of Technology, Beijing, China. [3]Beijing Key Lab of Nanophotonics and Ultrafine Optoelectronic Systems, Beijing Institute of Technology, Beijing, China. [4]CAS Key Laboratory of Theoretical Physics, Institute of Theoretical Physics, Chinese Academy of Sciences, Beijing, China. [5]Laboratory for Muon Spin Spectroscopy, Paul Scherrer Institute, Villigen PSI, Switzerland. [6]Laboratory for Quantum Emergence, Department of Physics, Southern University of Science and Technology, Shenzhen, China. [7]Quantum Science Center of Guangdong-Hong Kong-Macao Greater Bay Area (Guangdong), Shenzhen, China. [8]Material Science Center, Yangtze Delta Region Academy of Beijing Institute of Technology, Jiaxing, China. [9]Kavli Institute of Theoretical Sciences, University of Chinese Academy of Sciences, Beijing, China. [10]Trans-scale Quantum Science Institute, The University of Tokyo, Tokyo, Japan. [11]Beijing National Laboratory for Condensed Matter Physics and Institute of Physics, Chinese Academy of Sciences, Beijing, China. [12]Office of University Professor, The University of Tokyo, Kashiwa, Japan. [13]Material Innovation Research Center, The University of Tokyo, Kashiwa, Japan. [14]These authors contributed equally: Yigui Zhong, Jinjin Liu, Xianxin Wu. [15]Deceased: Shik Shin. ✉e-mail: zhiweiwang@bit.edu.cn; shixun@bit.edu.cn; okazaki@issp.u-tokyo.ac.jp

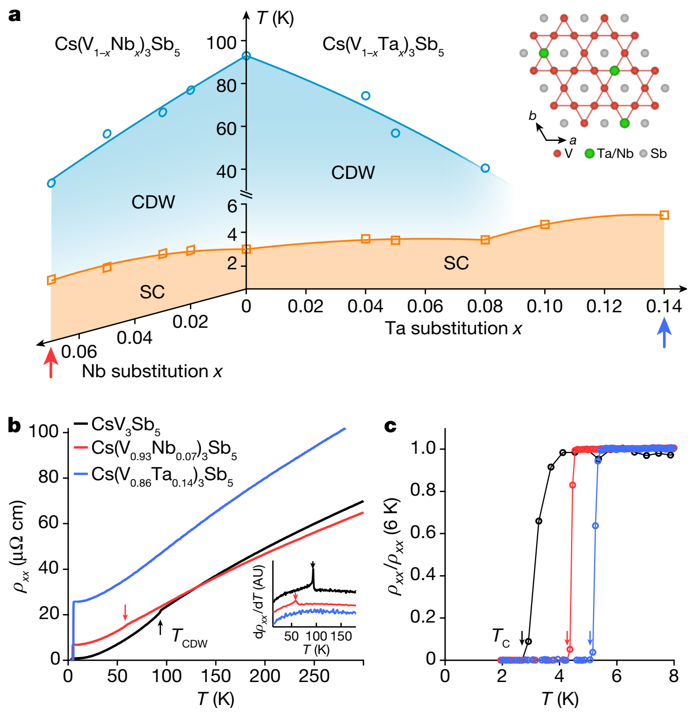

Fig. 1 | Evolution of CDW and superconductivity in CsV_3Sb_5 on chemical substitution. a, Phase diagrams for $Cs(V_{1-x}Nb_x)_3Sb_5$ and $Cs(V_{1-x}Ta_x)_3Sb_5$. Inset, the lattice structure of V–Sb layer, illustrating the Ta or Nb substitution of V atoms within the kagome lattice. **b**, Temperature dependence of in-plane resistivity for the pristine and two substituted samples studied in this work. The arrows indicate the anomalies associated with CDW transitions. The inset shows the differential resistivity to highlight the CDW transitions, with the curves vertically shifted for clarity. Note that there is no CDW order observed in $Cs(V_{0.86}Ta_{0.14})_3Sb_5$. **c**, Normalized resistivity curves in the low-temperature range showing clear superconducting transitions. AU, arbitrary unit.

photoemission spectroscopy (ARPES) has been proved to be a powerful tool to directly measure the SC gap in the momentum space[33]. Nevertheless, the relatively low transition temperature (T_c) and correspondingly small gap size render a thorough ARPES measurement extremely challenging.

In this work, we utilize an ultrahigh-resolution and low-temperature laser-ARPES, together with a chemical substitution of V in CsV_3Sb_5 that raises T_c, to precisely measure the gap structure in the superconducting state. CsV_3Sb_5 crystallizes in a layered structure with V atoms forming a two-dimensional kagome net, as shown in the inset of Fig. 1a. At low temperatures, the material exhibits a CDW transition at $T_{CDW} \approx 93$ K, and eventually becomes superconducting at $T_c \approx 3$ K. To finely tune the competition between superconductivity and CDW, we take two elements to substitute V in CsV_3Sb_5. As shown in Fig. 1, both substitutions show a similar trend in the phase diagram, but with distinctions—Nb substitution enhances T_c more efficiently, whereas Ta dopant concentration can be increased to fully suppress the CDW order. Considering the accessibility in terms of temperature and the possible influence of CDW, we select $Cs(V_{0.93}Nb_{0.07})_3Sb_5$ and $Cs(V_{0.86}Ta_{0.14})_3Sb_5$, from two typical regions in the phase diagram, for the SC gap measurement (denoted hereafter as Nb0.07 and Ta0.14, respectively). The Nb0.07 sample exhibits a T_c of 4.4 K and a T_{CDW} of 58 K, whereas the Ta0.14 sample exhibits a higher T_c of 5.2 K, but no clear CDW transition. Strikingly, as we shall present below, the gap structures of both samples are isotropic, regardless of the disappearance of CDW, hinting at a robust nodeless pairing in CsV_3Sb_5-derived kagome superconductors.

Spectroscopic evidence of the superconducting gap

Mapping out the Fermi surface (FS) is critical to investigate the SC gap structure, especially for a multiband system. Due to the limited detectable momentum area of the 5.8 eV laser source, Fig. 2a shows a joint FS of the Ta0.14 sample by combining three segments, which is validated by whole-FS mapping with a larger photon energy (Extended Data Fig. 1). Similar to the pristine CsV_3Sb_5 sample[6,34,35], the Ta0.14 sample has a circular electron-like pocket (marked as α) and a hexagonal hole-like pocket (marked as β) at the Brillouin zone (BZ) centre Γ point, and a triangle pocket (marked as δ) at the BZ corner K point. The α FS is formed by Sb 5*p* orbitals, whereas the β and δ FS are derived from V 3*d* orbitals[35] and are close in momentum. As shown in Figs. 2a and 3b, the β and δ FS are well distinguished due to the high momentum resolution of the laser source. Moreover, the intensities of the β and δ FS are enhanced under different polarizations of light (Extended Data Figs. 2 and 3, and see Methods for details), which further makes the determination of the Fermi momentum (k_F) reliable.

Before investigating the SC gap structure, we first present the spectral evidence of the superconductivity below T_c. Using the Ta0.14 sample as an example, the temperature-dependent energy distributed curves (EDCs) at k_F of a cut indicated in Fig. 2a are shown in Fig. 2b. At $T = 2$ K, far below the T_c, the emergence of the particle–hole symmetric quasiparticle peaks around the Fermi level (E_F) clearly indicate the opening of an SC gap. With temperature gradually increasing, the growing intensity at E_F and the approaching quasiparticle peaks suggest that the SC gap becomes smaller and eventually closes. Quantitatively, the SC gap amplitude can be extracted from the fitting procedure based on a Bardeen–Cooper–Schrieffer (BCS) spectral function (Methods). The inset of Fig. 2b summarizes the SC gap amplitudes $\Delta(T)$ at different temperatures, which fit well with the BCS-like temperature function. The fitted SC gap amplitude at zero temperature, Δ_0, is approximately 0.77 meV, and the estimated T_c of approximately 5.2 K is consistent with the bulk T_c determined by resistivity measurements (Fig. 1c). These results demonstrate the high quality of the samples and the high precision of our SC gap measurements.

Superconducting gap structure in CDW-suppressed $Cs(V_{0.86}Ta_{0.14})_3Sb_5$

We then study the momentum dependence of the SC gap in the Ta0.14 sample, in which the CDW order is fully suppressed (Fig. 1b). Considering the six-fold symmetry of the FS, we select various k_F points to cover the complete FS sheets and thus capture the symmetry of the SC gap, as shown in Fig. 2f. The EDCs at k_F of the α, β and δ Fermi surfaces are presented in Fig. 2c–e. For each k_F point, we take spectra below and above T_c, to ensure a precise in situ comparison. In the vicinity of E_F, the leading edge of the EDCs at 2 K all show a shift compared to that at 7 K. Moreover, they universally show a strong coherence peak at a binding energy E_B of approximately 1 meV, indicating a rather isotropic SC gap structure. Fitting these EDCs to a BCS spectral function, the quantitatively extracted SC gap amplitudes are summarized in Fig. 2g. These SC gaps of different Fermi surfaces have rarely fluctuated amplitudes with an average Δ_{Ta} of 0.77 ± 0.06 meV, yielding a ratio $2\Delta_{Ta}/k_BT_c$ of 3.44 ± 0.27 (where k_B is the Boltzmann constant; Extend Data Table 1), which is close to the BCS value of approximately 3.53. These results clearly demonstrate an isotropic SC gap in the Ta0.14 sample.

Superconducting gap structure in charge-ordered $Cs(V_{0.93}Nb_{0.07})_3Sb_5$

Next, we turn to examine the possible influence of the CDW order in the normal state on the superconducting pairing symmetry[16,29,30]. We measure the SC gap structure of the Nb0.07 sample, where T_{CDW} gets slightly suppressed, and T_c smoothly increases from that of the pristine

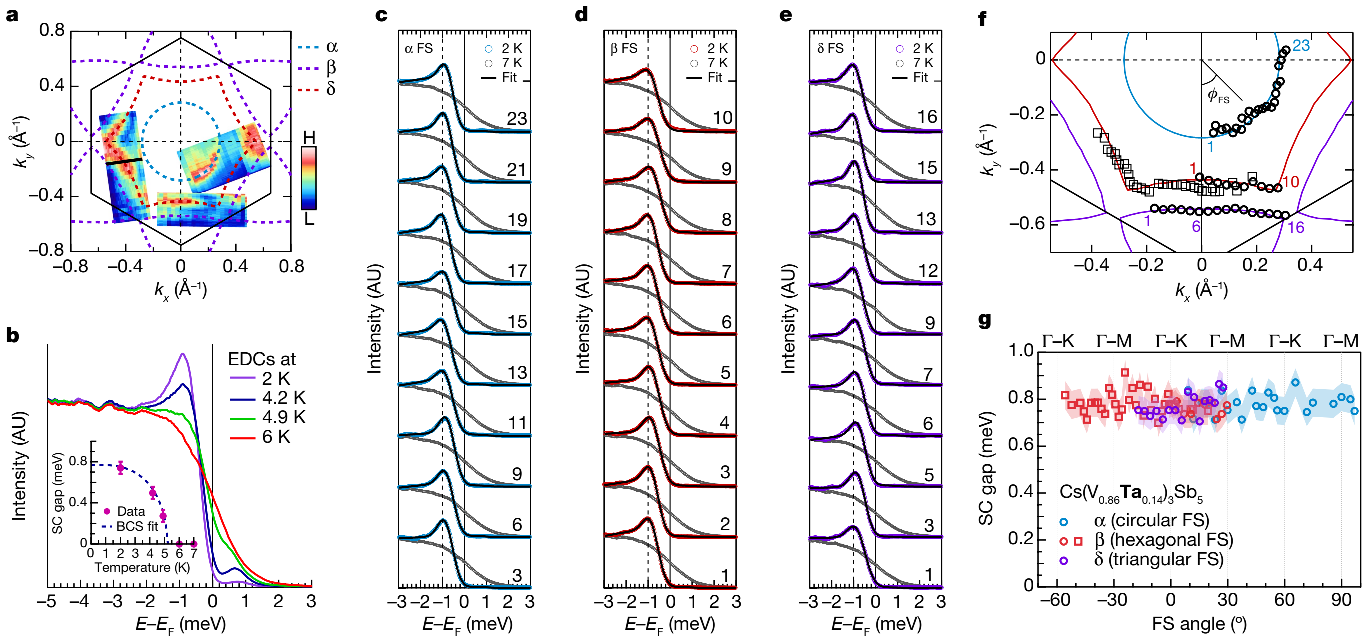

Fig. 2 | Isotropic superconducting gap in $Cs(V_{0.86}Ta_{0.14})_3Sb_5$. **a**, ARPES intensity integrated over ±5 meV around E_F. The broken lines represent the FS contours. **b**, Temperature dependence of EDC at k_F in a cut marked as a black line in **a**. Inset, temperature-dependent SC gap amplitude determined by the fitting procedure based on the BCS spectral function. The blue broken curve represents BCS-like temperature dependence. **c**–**e**, EDCs at k_F measured at $T = 2$ K and 7 K along with the α (**c**), β (**d**) and δ (**e**) FS, respectively. **f**, Summary of the k_F positions of the EDCs shown in **c**–**e**, shown as black thick circles. The black lines are the curves fitted by the BCS spectral function. The dashed lines mark the peak of the EDCs. **g**, SC gap amplitude estimated from the fits to EDCs shown in **c**–**e**. The shaded areas represent the error bars determined from the standard deviation of E_F. The square makers are the SC gap results from an independent sample and the corresponding k_F are shown as thin squares in **f**.

CsV_3Sb_5 (Fig. 1a). In this sense, the superconductivity in the Nb0.07 sample is expected to have a similar SC gap structure to CsV_3Sb_5. As shown in Fig. 3a, the FS topology of the Nb0.07 sample is also similar to that of CsV_3Sb_5, consisting of the circular α FS, hexagonal β FS and triangular δ FS, which is consistent with the helium-lamp-based ARPES measurements (Extended Data Fig. 1) and the calculations based on

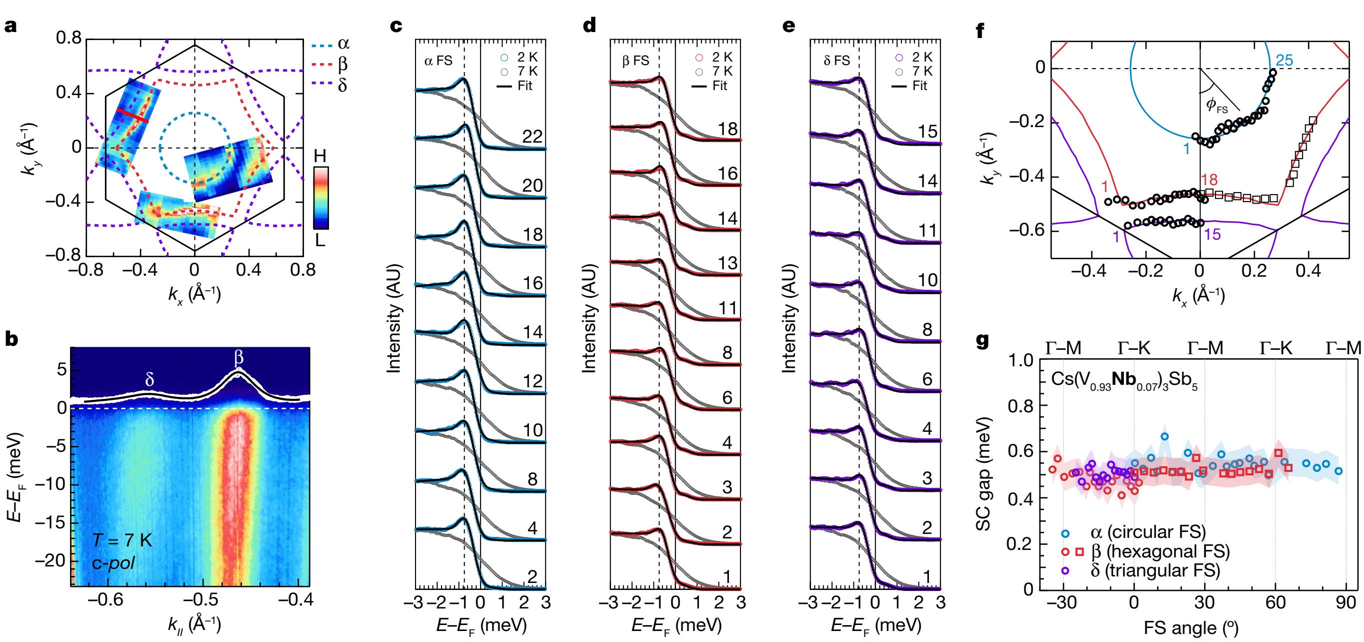

Fig. 3 | Isotropic superconducting gap in charge-ordered $Cs(V_{0.93}Nb_{0.07})_3Sb_5$. **a**, ARPES intensity integrated over ±5 meV around E_F. The broken lines represent the FS contours. **b**, ARPES intensity plot along a red line shown in **a**. The intensity is measured using circular polarization to capture both β and δ bands. The white dotted line represents the MDC integrated over ±2 meV around E_F and the black line is a double-peak Lorentzian fit. Two peaks distinguished in the MDC show k_F positions of the β and δ bands. **c**–**e**, EDCs at k_F taken along the α (**c**), β (**d**) and δ (**e**) FS, respectively. **f**, Summary of the k_F positions of the EDCs in **c**–**e**. The black lines are the curves fitted by the BCS spectral function. The dashed lines mark the estimated peak position of the EDCs. **g**, SC gap amplitude estimated from the fits to EDCs shown in **c**–**e**. The square makers are the SC gap results from an independent sample and the corresponding k_F are shown as thin squares in **f**. The shaded areas represent the error bars determined from the standard deviation of E_F.

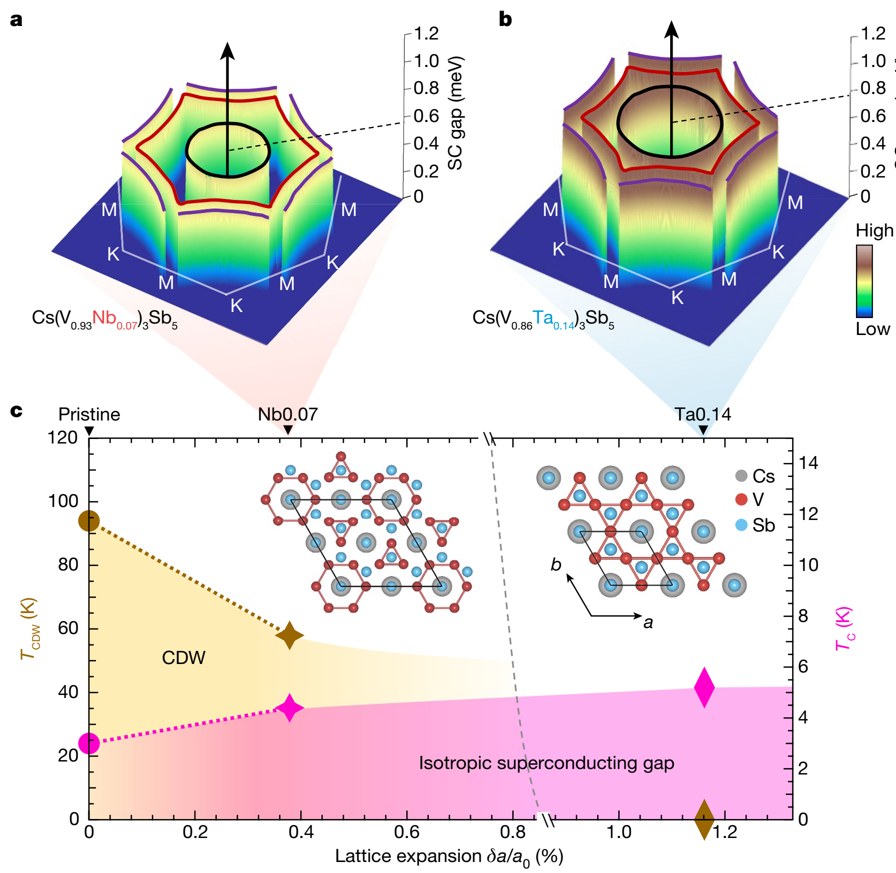

Fig. 4 | Robust isotropic SC gap on suppression of CDW. a,**b**, Schematic momentum dependence of the SC gap amplitude of the Nb0.07 (**a**) and Ta0.14 (**b**) samples, respectively. **c**, Schematic phase diagram in which T_{CDW} and T_c are plotted as a function of the lattice expansion due to the chemical substitutions. The lattice expansion is represented by $\delta a/a_0$, where $\delta a = a - a_0$ is the change of the in-plane lattice constant (a) from that of pristine CsV_3Sb_5 (a_0). The inset shows the lattice structures of the CDW (left) and undistorted (right) phases, representing the states above T_c for two distinct regions in the phase diagram. The black solid lines in the insets mark the corresponding single-unit cells. The isotropic SC gap symmetry persists through two such regions, regardless of the existence of CDW order.

density function theory[36]. The EDCs at k_F positions indicated in Fig. 3f, on these three Fermi surfaces, are presented in Fig. 3c–e. Just like the case for the Ta0.14 sample, coherence peaks arise at a similar energy position for all EDCs at 2 K, albeit of a slightly broader shape due to a smaller SC gap and lower T_c. By fitting the EDCs to the BCS spectral function, the SC gap amplitudes along the Fermi surfaces are summarized in Fig. 3g. The data clearly show a nearly isotropic SC gap structure in the Nb0.07 sample, with the gap amplitude Δ_{Nb} of 0.54 ± 0.06 meV, giving a ratio $2\Delta_{Nb}/k_BT_c$ of 2.83 ± 0.32 (Extended Data Table 2), which is smaller than the BCS value. Our results show that an isotropic SC gap robustly persists in the Nb0.07 sample with CDW order.

As the kagome metals AV_3Sb_5 have a three-dimensional electronic structure[34,35], we further study the *z*-direction momentum (k_z) dependence of the SC gap by tuning the photon energy from 5.8 eV to 7 eV. We find that the SC gap remains nearly the same at these two k_z planes within our experimental uncertainties (Extended Data Fig. 4). Giving the direct momentum-resolving capability of ARPES and the prominent features of SC gap opening, our data reveal a nodeless, nearly isotropic and orbital-independent SC gap in both Nb0.07 and Ta0.14 samples (Fig. 4a,b).

Discussions and perspectives

These results shine a light on the interplay between superconductivity and CDW in CsV_3Sb_5. As shown in Fig. 4c and Extended Data Fig. 5, the isovalent substitutions of Nb/Ta for V in our experiments can be viewed as an effective in-plane negative pressure, which suppresses the CDW order while it enhances the superconductivity. In the absence of the CDW order, our measurements on the Ta0.14 sample reveal a nearly isotropic gap structure (Fig. 4b). When the CDW order associated with an anisotropic gap[34,37] comes into play in the Nb0.07 sample, the SC gap remains isotropic and nodeless (Fig. 4a), different from the muon spin relaxation (μSR) observation of a nodal-to-nodeless transition in the sister compounds KV_3Sb_5 and RbV_3Sb_5 under hydrostatic pressure[16]. The difference between the two regimes, represented by the Nb0.07 and Ta0.14 samples, is that the ratio $2\Delta/k_BT_c$ is smaller when superconductivity emerges inside the CDW order. This may be attributed to the CDW order partially gapping out the Fermi surfaces and generating spin polarizations before entering the superconducting phase.

We further discuss the pairing symmetry in CsV_3Sb_5-derived kagome superconductors. Although the SC gap structure in pristine CsV_3Sb_5 with a relatively low T_c is not examined, the nodeless gap is probably retained according to the similarities between the pristine and Nb0.07 samples in terms of electronic structure (Extended Data Figs. 1, 7 and 8), charge ordering and transport properties (Fig. 4c). The robust isotropic SC gaps with small $2\Delta/k_BT_c$ in the presence or absence of the CDW seem to be consistent with a conventional s-wave pairing. This is also supported by the observed band dispersion kinks[37,38] stemming from a non-negligible electron–phonon coupling, as well as the positive correlation between the coupling strength and T_c (Extended Data Fig. 6). Precisely, these results do not rule out other nodeless pairing states due to the lack of phase information in ARPES measurements.

Recent μSR studies[25,39] report a possible time-reversal symmetry breaking associated with the CDW state in CsV_3Sb_5 and the SC state in pressurized CsV_3Sb_5. Additionally, our recent μSR measurements on the CDW-suppressed Ta0.14 sample, which will be published elsewhere, also provide evidence for the potential presence of time-reversal symmetry-breaking superconductivity, highlighting the need for further examination. Our direct determination of the robust isotropic SC gap significantly narrows down the pairing symmetry and offers crucial insights into the pairing mechanism, thus laying a foundation for deciphering the nature of the superconductivity and its intertwined orders in these kagome quantum materials.

Online content

Any methods, additional references, Nature Portfolio reporting summaries, source data, extended data, supplementary information, acknowledgements, peer review information; details of author contributions and competing interests; and statements of data and code availability are available at https://doi.org/10.1038/s41586-023-05907-x.

1. Syôzi, I. Statistics of kagomé lattice. *Prog. Theor. Phys.* **6**, 306–308 (1951).
2. Yu, S.-L. & Li, J.-X. Chiral superconducting phase and chiral spin-density-wave phase in a Hubbard model on the kagome lattice. *Phys. Rev. B* **85**, 144402 (2012).
3. Kiesel, M. L., Platt, C. & Thomale, R. Unconventional Fermi surface instabilities in the kagome Hubbard model. *Phys. Rev. Lett.* **110**, 126405 (2013).
4. Wang, W.-S., Li, Z.-Z., Xiang, Y.-Y. & Wang, Q.-H. Competing electronic orders on kagome lattices at van Hove filling. *Phys. Rev. B* **87**, 115135 (2013).
5. Ortiz, B. R. et al. New kagome prototype materials: discovery of KV_3Sb_5, RbV_3Sb_5, and CsV_3Sb_5. *Phys. Rev. Mater.* **3**, 094407 (2019).
6. Ortiz, B. R. et al. CsV_3Sb_5: a Z_2 topological kagome metal with a superconducting ground state. *Phys. Rev. Lett.* **125**, 247002 (2020).
7. Yin, J.-X., Lian, B. & Hasan, M. Z. Topological kagome magnets and superconductors. *Nature* **612**, 647–657 (2022).
8. Jiang, Y.-X. et al. Unconventional chiral charge order in kagome superconductor KV_3Sb_5. *Nat. Mater.* **20**, 1353–1357 (2021).
9. Mielke, C. et al. Time-reversal symmetry-breaking charge order in a kagome superconductor. *Nature* **602**, 245–250 (2022).
10. Chen, H. et al. Roton pair density wave in a strong-coupling kagome superconductor. *Nature* **599**, 222–228 (2021).
11. Xu, H.-S. et al. Multiband superconductivity with sign-preserving order parameter in kagome superconductor CsV_3Sb_5. *Phys. Rev. Lett.* **127**, 187004 (2021).
12. Zhao, C. et al. Nodal superconductivity and superconducting domes in the topological Kagome metal CsV_3Sb_5. Preprint at https://doi.org/10.48550/arXiv.2102.08356 (2021).
13. Mu, C. et al. S-wave superconductivity in kagome metal CsV_3Sb_5 revealed by $^{121/123}$Sb NQR and ^{51}V NMR measurements. *Chin. Phys. Lett.* **38**, 077402 (2021).
14. Duan, W. et al. Nodeless superconductivity in the kagome metal CsV_3Sb_5. *Sci. China Phys. Mech. Astron.* **64**, 107462 (2021).
15. Gupta, R. et al. Microscopic evidence for anisotropic multigap superconductivity in the CsV_3Sb_5 kagome superconductor. *npj Quantum Mater.* **7**, 49 (2022).
16. Guguchia, Z. et al. Tunable nodal kagome superconductivity in charge ordered RbV_3Sb_5. *Nat. Commun.* **14**, 153 (2022).
17. Lou, R. et al. Charge-density-wave-induced peak-dip-hump structure and the multiband superconductivity in a kagome superconductor CsV_3Sb_5. *Phys. Rev. Lett.* **128**, 036402 (2022).
18. Wu, X. et al. Nature of unconventional pairing in the kagome superconductors AV_3Sb_5 (A=K, Rb, Cs). *Phys. Rev. Lett.* **127**, 177001 (2021).
19. Tazai, R., Yamakawa, Y., Onari, S. & Kontani, H. Mechanism of exotic density-wave and beyond-Migdal unconventional superconductivity in kagome metal AV_3Sb_5 (A=K, Rb, Cs). *Sci. Adv.* **8**, eabl4108 (2022).
20. Gu, Y., Zhang, Y., Feng, X., Jiang, K. & Hu, J. Gapless excitations inside the fully gapped kagome superconductors AV_3Sb_5. *Phys. Rev. B* **105**, L100502 (2022).
21. Keimer, B., Kivelson, S. A., Norman, M. R., Uchida, S. & Zaanen, J. From quantum matter to high-temperature superconductivity in copper oxides. *Nature* **518**, 179–186 (2015).
22. Fernandes, R. M. et al. Iron pnictides and chalcogenides: a new paradigm for superconductivity. *Nature* **601**, 35–44 (2022).
23. He, R.-H. et al. Energy gaps in the failed high-T_c superconductor $La_{1.875}Ba_{0.125}CuO_4$. *Nat. Phys.* **5**, 119–123 (2009).
24. Neupert, T., Denner, M. M., Yin, J.-X., Thomale, R. & Hasan, M. Z. Charge order and superconductivity in kagome materials. *Nat. Phys.* **18**, 137–143 (2021).
25. Khasanov, R. et al. Time-reversal symmetry broken by charge order in CsV_3Sb_5. *Phys. Rev. Res.* **4**, 023244 (2022).
26. Xu, Y. et al. Three-state nematicity and magneto-optical Kerr effect in the charge density waves in kagome superconductors. *Nat. Phys.* **18**, 1470–1475 (2022).
27. Xiang, Y. et al. Twofold symmetry of *c*-axis resistivity in topological kagome superconductor CsV_3Sb_5 with in-plane rotating magnetic field. *Nat. Commun.* **12**, 6727 (2021).
28. Li, H. et al. Rotation symmetry breaking in the normal state of a kagome superconductor KV_3Sb_5. *Nat. Phys.* **18**, 265–270 (2022).
29. Chen, K. et al. Double superconducting dome and triple enhancement of T_c in the kagome superconductor CsV_3Sb_5 under high pressure. *Phys. Rev. Lett.* **126**, 247001 (2021).
30. Yu, F. et al. Unusual competition of superconductivity and charge-density-wave state in a compressed topological kagome metal. *Nat. Commun.* **12**, 3645 (2021).
31. Yang, S.-Y. et al. Giant, unconventional anomalous Hall effect in the metallic frustrated magnet candidate, KV_3Sb_5. *Sci. Adv.* **6**, eabb6003 (2020).
32. Yu, F. et al. Concurrence of anomalous Hall effect and charge density wave in a superconducting topological kagome metal. *Phys. Rev. B* **104**, L041103 (2021).
33. Sobota, J. A., He, Y. & Shen, Z.-X. Angle-resolved photoemission studies of quantum materials. *Rev. Mod. Phys.* **93**, 025006 (2021).
34. Kang, M. et al. Twofold van Hove singularity and origin of charge order in topological kagome superconductor CsV_3Sb_5. *Nat. Phys.* **18**, 301–308 (2022).
35. Hu, Y. et al. Rich nature of Van Hove singularities in Kagome superconductor CsV_3Sb_5. *Nat. Commun.* **13**, 2220 (2022).
36. Li, Y. et al. Tuning the competition between superconductivity and charge order in the kagome superconductor $Cs(V_{1-x}Nb_x)_3Sb_5$. *Phys. Rev. B* **105**, L180507 (2022).
37. Luo, H. et al. Electronic nature of charge density wave and electron-phonon coupling in kagome superconductor KV_3Sb_5. *Nat. Commun.* **13**, 273 (2022).
38. Zhong, Y. et al. Testing electron-phonon coupling for the superconductivity in kagome metal CsV_3Sb_5. Preprint at https://doi.org/10.48550/arXiv.2207.02407 (2022).
39. Gupta, R. et al. Two types of charge order with distinct interplay with superconductivity in the kagome material CsV_3Sb_5. *Commun. Phys.* **5**, 232 (2022).

Methods

Growth of single crystals

High-quality single crystals of $Cs(V_{0.86}Ta_{0.14})_3Sb_5$ and $Cs(V_{0.93}Nb_{0.07})_3Sb_5$ were synthesized from Cs bulk (Alfa Aesar, 99.8%), V pieces (Aladdin, 99.97%), Ta powder (Alfa Aesar, 99.99%) and Sb shot (Alfa Aesar, 99.9999%) via a self-flux method using $Cs_{0.4}Sb_{0.6}$ as the flux. The above starting materials were put into an aluminium crucible and sealed in a quartz tube, which was then heated to 1,000 °C in 24 h and maintained for 200 h. After that, the tube was cooled to 200 °C at a rate of 3 °C h^{-1}, followed by cooling down to room temperature with the furnace switched off. To remove the flux, the obtained samples were soaked in deionized water. Finally, shiny single crystals with hexagonal features were obtained.

Electronic transport measurements

Electronic transport properties of $Cs(V_{0.86}Ta_{0.14})_3Sb_5$ and $Cs(V_{0.93}Nb_{0.07})_3Sb_5$ crystals were measured on a physical property measurement system (Quantum Design) at a temperature range from 300 K to 1.8 K. A five-terminal method was used, at which the longitudinal resistivity and Hall resistivity can be taken simultaneously. The direct current magnetic susceptibility was measured on a magnetic property measurement system (Quantum Design) with a superconducting quantum interference device magnetometer.

High-resolution laser-ARPES measurements

Ultrahigh-resolution ARPES measurements were performed in a laser-based ARPES setup, which consisted of a continuous wave laser ($h\upsilon$ = 5.8 eV) provided from OXIDE Corporation and a vacuum ultraviolet laser[40] ($h\upsilon$ = 6.994 eV, called '7 eV' for convenience), a Scienta HR8000 hemispherical analyser and a sample manipulator cooled by decompression-evaporation of the liquid helium. The samples were cleaved in situ and measured under a vacuum better than 3×10^{-11} torr. The sample temperature was varied from 2 to 7 K, and the energy resolution for the superconducting gap measurements was better than 0.6 meV for the 5.8 eV laser, and 1.5 meV for the 6.994 eV laser. We checked the linearity of the detector[41], and the Fermi level E_F was calibrated with an in situ connected gold reference.

Summary of Fermi surface and identification of k_F

The FS was obtained by integrating the ARPES intensity over ±5 meV around E_F. Due to the limited detectable momentum area of the 5.8 eV laser source, we measured multiple samples to cover all the FS contours. We summarize the FS maps of the measured samples and the corresponding k_F points in Extended Data Figs. 2 and 3 for $Cs(V_{0.86}Ta_{0.14})_3Sb_5$ (denoted as Ta0.14) and $Cs(V_{0.93}Nb_{0.07})_3Sb_5$ (denoted as Nb0.07), respectively. The k_F was determined directly from the peak position of the integrated momentum distributed curve (MDC) at $T > T_c$ over $E_F \pm 2$ meV (white dotted line in Fig. 3b). The peak position was obtained from a Lorentzian fit. It is worth noting that although the β and δ Fermi surfaces are close in momentum, the corresponding bands can be well distinguished. As shown in Extended Data Figs. 2b–d and 3b–d, the intensity of the β and δ bands are enhanced under different polarizations due to different V 3*d* orbital characters—*s* polarization for the β FS and *p* polarization for the δ FS.

Fitting procedure to obtain the amplitude of the SC gap

The SC gap amplitude was quantitatively determined by the fits based on the BCS spectral function[42–44], which has the form

$$A_{\mathrm{BCS}}(k,\omega) = \frac{1}{\pi}\left[\frac{|u_k|^2\Gamma}{(\omega - \sqrt{\varepsilon_k^2 + |\Delta(k)|^2})^2 + \Gamma^2} + \frac{|v_k|^2\Gamma}{(\omega + \sqrt{\varepsilon_k^2 + |\Delta(k)|^2})^2 + \Gamma^2}\right] \quad (1)$$

where $|u_k|^2$ and $|v_k|^2$ are coherence factors for the occupied and unoccupied quasiparticles, respectively, Γ is the line width broadening factor due to the finite quasiparticle lifetime, $E_k = \sqrt{\varepsilon_k^2 + |\Delta(k)|^2}$ is the Bogoliubov quasiparticle band dispersion, ε_k is the band dispersion near E_F in the normal state and $|\Delta(k)|$ is the SC gap amplitude. To fit the ARPES data, the BCS spectral function is multiplied by the Fermi–Dirac function and convoluted with a Gaussian function corresponding to the experimental energy resolution. Then, the EDCs at k_F, obtained by integrating the ARPES intensity over $k_F \pm 0.02$ Å^{-1}, were fitted to extract the SC gap $|\Delta(k)|$.

Statistics of the fitted SC gap amplitude measured on different samples

By applying the fitting procedure to the EDCs at k_F on the different Fermi surfaces, we obtain the momentum dependence of the SC gap amplitude, which directly reflects the pairing symmetry. As presented in Figs. 2g and 3g in the main text, we observed that the SC gap amplitudes of both the Ta0.14 and Nb0.07 samples are nearly isotropic in the momentum space. To demonstrate the small fluctuation of the SC gap amplitudes, we present the statistics of the fitted SC gap amplitudes for the Ta0.14 samples in Extended Data Table 1, and for the Nb0.07 samples in Extended Data Table 2. The average deviations are less than 0.04 meV, which means a very small fluctuation around the average value of the SC gap amplitude ($\overline{\Delta}$). Moreover, the difference between the maximum and minimum values of the SC gap amplitudes, $\Delta_{max} - \Delta_{min}$, is comparable to two times the standard deviation of E_F (approximately 0.06 meV), which determines the error bars for the SC gap. These demonstrate that the SC gap amplitude is almost constant in different momenta, supporting a nearly isotropic pairing gap structure. The consistent SC gap observed in different samples demonstrates the high quality of the single crystals and excludes sample-dependent influences on the SC gap.

Superconducting gap at difference k_z

The FS maps of the Nb0.07 sample measured with 5.8 eV and 7 eV lasers are plotted in Extended Data Fig. 4a,d. Here we apply an inner potential of 7.3 eV (ref. 45) to calculate k_z for different $k_{//}$, as shown in the inset of Extended Data Fig. 4g. The EDCs at k_F on the β FS are shown in Extended Data Fig. 4b for the 5.8 eV laser and Extended Data Fig. 4e for the 7 eV laser. The corresponding symmetrized EDCs are shown in Extended Data Fig. 4c,f. Because the energy resolution for the measurements with the 7 eV laser is about twice as large as that with the 5.8 eV laser, the coherence peak of the EDCs measured with the 7 eV laser is broader than that measured with the 5.8 eV laser. To effectively compare the SC gap at these two different k_z, the EDCs were fitted with equation (1), with the energy resolution taken into account. The extracted SC gap amplitudes at these two k_z planes are summarized in Extended Data Fig. 4g, which clearly shows that they are nearly the same within experimental uncertainties, implying a nearly isotropic SC gap along the k_z direction.

Spectral evidence of electron–phonon coupling

Electron–phonon coupling (EPC) is ubiquitous in quantum materials, which could induce kinks in the band dispersion at the frequencies of the coupled phonons[46,47]. As shown in Extended Data Fig. 6a–c, kinks are observed on the α and β bands for all the pristine, Nb0.07 and Ta0.14 samples. These kinks are more prominent in the extracted band dispersions from the fits of the MDCs, as shown in Extended Data Fig. 6d–f. For the α band, the kink is at the binding energy E_B of approximately 30 meV, whereas for the β band two kinks are distinguished at E_B of approximately 10 meV and 30 meV. The EPC is enhanced for the Nb0.07 and Ta0.14 samples, which have a higher T_c compared to the pristine sample. The EPC strength can be roughly estimated by the ratio between the Fermi velocity and the velocity of the bare band[47,48]. Here the bare band is the band dispersion without the effect of EPC, which is assumed as a line between a high E_B and E_F. As shown in Extended Data Fig. 6g, with the V partially substituted by the Nb/Ta, the EPC strength on the β band (derived from V 3*d* orbitals) is prominently enhanced, whereas the EPC strength on the α band (derived from Sb 5*p* orbitals) remains nearly constant. Such enhancements of EPC in the samples with higher T_c suggest an important role of the EPC in promoting the superconductivity of the CsV_3Sb_5 family of materials.

Evolution of the van Hove singularities via Nb/Ta substitutions

We performed additional ARPES measurements to study the evolution of van Hove singularities (VHS) in the pristine CsV_3Sb_5, Nb0.07 and Ta0.14 samples. To avoid the influence of the CDW gap, the ARPES spectra were taken in the normal state (above the T_{CDW}) along the K–M–K direction. As shown in Extended Data Fig. 7, one can find that the energy positions of the VHS show a moderate shift, whereas the corresponding superconducting gaps are always isotropic and nodeless. Such a shift of VHS is consistent with our density functional theory calculations shown in Extended Data Fig. 8. We note that two VHS can be distinguished around E_F at low temperatures[34,35], although only one VHS is observed here at high temperatures. Theoretically, although there are multiple VHS near the Fermi level, and electronic interactions may generate pairings with close pairing strengths, the further inclusion of electron–phonon coupling, experimentally evidenced by the band kinks shown in Extended Data Fig. 6, may lift the quasi-degeneracy and one pairing may always be dominant. Therefore, the variation of the energy position of VHS should have little effect on the pairing symmetry in realistic materials. Despite this, the unique sublattice feature at van Hove fillings and enhanced non-local electronic interactions in the kagome lattice can play an important role in generating unconventional pairing[2–4].

Data availability

Data are available from the corresponding author upon reasonable request.

40. Shimojima, T., Okazaki, K. & Shin, S. Low-temperature and high-energy-resolution laser photoemission spectroscopy. *J. Phys. Soc. Jpn* **84**, 072001 (2015).
41. Reber, T., Plumb, N., Waugh, J. & Dessau, D. Effects, determination, and correction of count rate nonlinearity in multi-channel analog electron detectors. *Rev. Sci. Instrum.* **85**, 043907 (2014).
42. Matsui, H. et al. BCS-like Bogoliubov quasiparticles in high-T_c superconductors observed by angle-resolved photoemission spectroscopy. *Phys. Rev. Lett.* **90**, 217002 (2003).
43. Shimojima, T. et al. Orbital-independent superconducting gaps in iron pnictides. *Science* **332**, 564–567 (2011).
44. Okazaki, K. et al. Octet-line node structure of superconducting order parameter in KFe_2As_2. *Science* **337**, 1314–1317 (2012).
45. Li, C. et al. Coexistence of two intertwined charge density waves in a kagome system. *Phys. Rev. Res.* **4**, 033072 (2021).
46. Valla, T., Fedorov, A. V., Johnson, P. D. & Hulbert, S. L. Many-body effects in angle-resolved photoemission: quasiparticle energy and lifetime of a Mo(110) surface state. *Phys. Rev. Lett.* **83**, 2085–2088 (1999).
47. Lanzara, A. et al. Evidence for ubiquitous strong electron–phonon coupling in high-temperature superconductors. *Nature* **412**, 510–514 (2001).
48. Johnson, P. et al. Doping and temperature dependence of the mass enhancement observed in the cuprate $Bi_2Sr_2CaCu_2O_{8+\delta}$. *Phys. Rev. Lett.* **87**, 177007 (2001).

Acknowledgements We thank W. Zhang, S. Huh and M. Liu for stimulating discussions. This work was supported by the National Key Research and Development Program of China (grant nos 2020YFA0308800 and 2022YFA1403400), the Grants-in-Aid for Scientific Research (KAKENHI) (grant nos JP18K13498, JP19H01818, JP19H00651 and JP21H04439) from the Japan Society for the Promotion of Science (JSPS), JSPS KAKENHI on Innovative Areas 'Quantum Liquid Crystals' (grant no. JP19H05826), the Center of Innovation Program from the Japan Science and Technology Agency (JST) and MEXT Quantum Leap Flagship Program of Japan (MEXT Q-LEAP) (grant no. JPMXS0118068681), the National Science Foundation of China (grant nos 12061131002, 12234003 and 92065109),. and the Beijing Natural Science Foundation (grant nos Z210006 and Z190006). X.S. was supported by the Beijing Institute of Technology (BIT) Research Fund Program for Young Scholars. Z.W. thanks the Analysis and Testing Center at BIT for assistance in facility support. J.-X.Y. was supported by South University of Science and Technology of China principal research grant (no. Y01202500). X.H. acknowledges the support from the China Postdoctoral Science Foundation Fellowship (no. 2022M723112). J.H. was supported by the Ministry of Science and Technology of China (grant no. 2022YFA1403901) and the National Natural Science Foundation of China (grant no. NSFC-1188810).

Author contributions Y.Z., X.S. and K.O. conceived the project. Y.Z. performed the ARPES experiments with assistance from A.M., S.N., T.S. and K.L., and with guidance from T.K. and K.O. Z.G., J.-X.Y., D.D., C.M.III, R.K. and H.L. contributed to interpretation of data and making a conclusion. J.L., Y.L. and Z.W. grew the samples and performed sample characterizations. X.W. performed the band calculations. X.W., X.H. and J.H. contributed to theoretical inputs. Y.Z., X.S., X.W., J.-X.Y. and K.O. prepared the manuscript with input from all authors.

Competing interests The authors declare no competing interests.

Additional information

Correspondence and requests for materials should be addressed to Zhiwei Wang, Xun Shi or Kozo Okazaki.

Peer review information *Nature* thanks Myung Joon Han and the other, anonymous, reviewer(s) for their contribution to the peer review of this work.

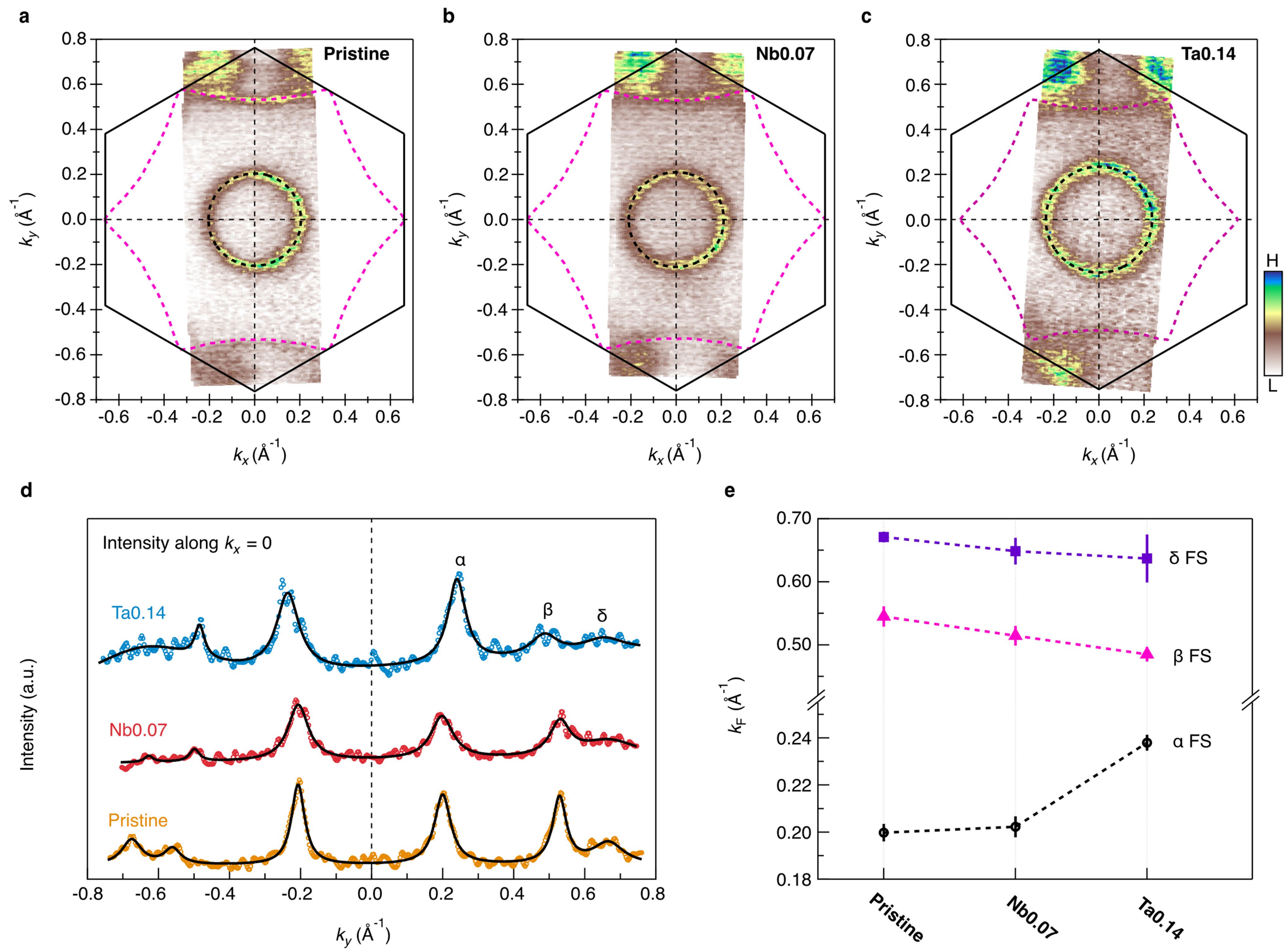

Extended Data Fig. 1 | Fermi surface evolution upon Nb/V substitutions. **a**–**c**, Fermi surface maps integrated over $E_F \pm 5$ meV for the pristine, 7%-Nb and 14%-Ta substituted CsV_3Sb_5 samples, respectively. The spectra were measured with He Iα photons (hν = 21.218 eV) at T = 7 K. **d**, Line cuts along k_x = 0. The black lines are the Lorentizen fits to determine the k_F positions. **e**, Summary of the k_F evolution of three Fermi surfaces upon Nb/V substitutions. The error bars represent the uncertainties of the fits.

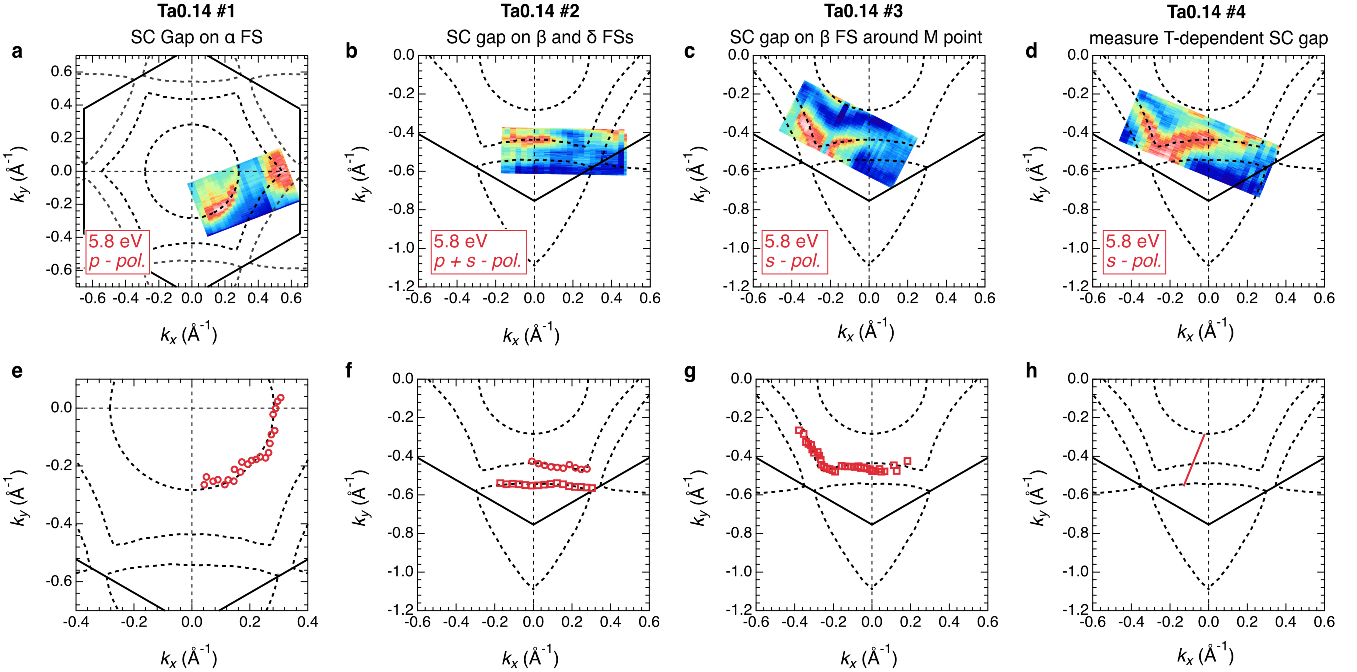

Extended Data Fig. 2 | Fermi surfaces of all measured Ta0.14 samples. a–d, ARPES intensity integrated over $E_F \pm 5$ meV. **e–h**, k_F points at which the superconducting gap is measured.

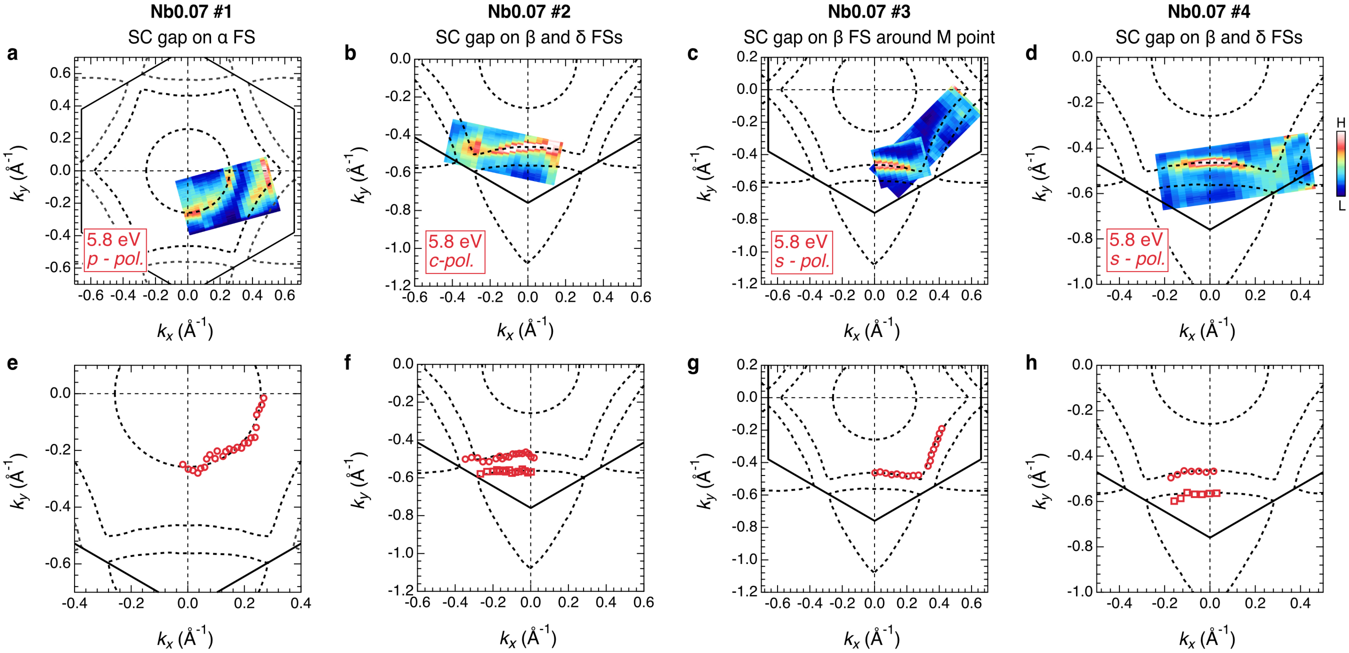

Extended Data Fig. 3 | Fermi surfaces of all measured Nb0.07 samples. a–d, ARPES intensity integrated over $E_F \pm 5$ meV. **e–h**, k_F points at which the superconducting gap is measured.

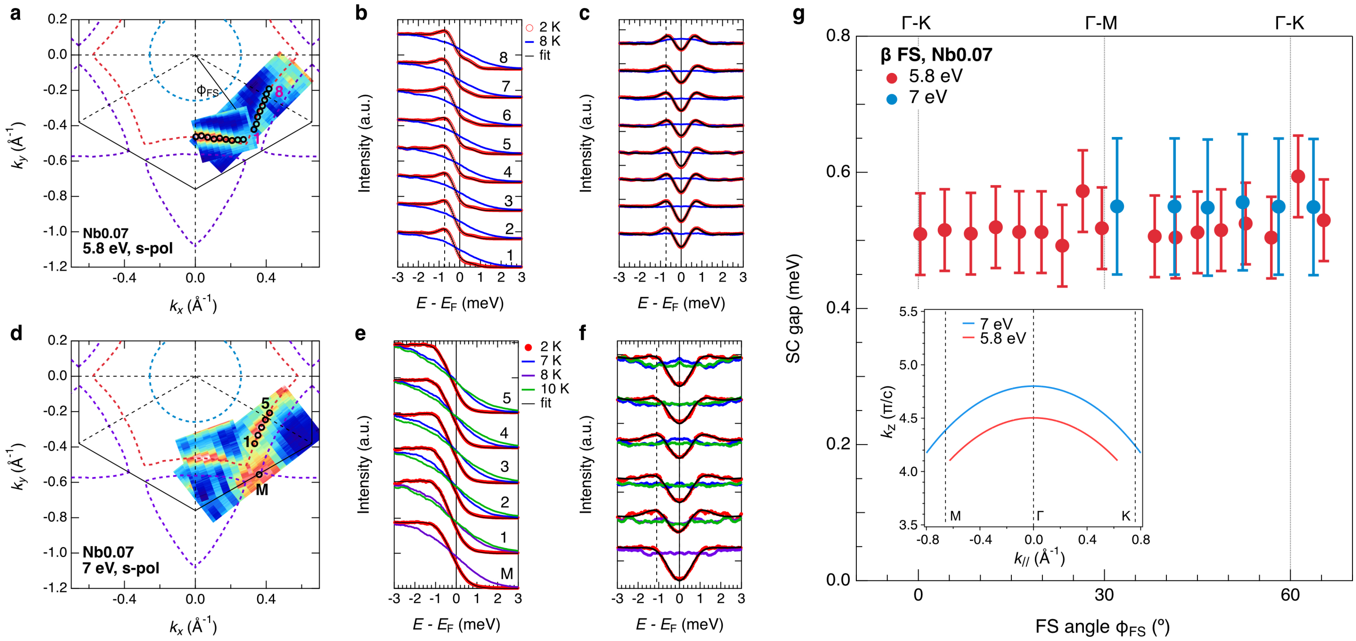

Extended Data Fig. 4 | Superconducting gap at different k_z for the $Cs(V_{0.93}Nb_{0.07})_3Sb_5$ sample. a, FS map taken with 5.8-eV laser. **b**, EDCs at k_F marked in **a**. The black lines are the fits of these EDCs. **c**, Symmetrized EDCs for **b**. **d–f**, Same as a-c but for the data taken with 7-eV laser. The curves are vertically offset for clarity. **g**. Comparison of the SC gap amplitude measured with 5.8-eV and 7-eV laser. The inset shows the k_z positions corresponding to these two photon energies.

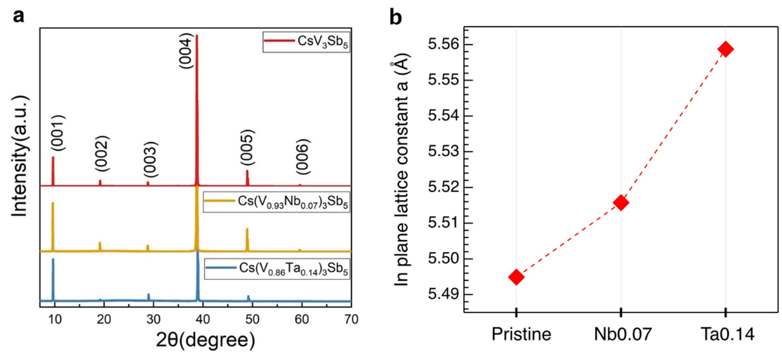

Extended Data Fig. 5 | X-ray diffraction (XRD) measurements. a, XRD of the pristine CsV_3Sb_5, Nb0.07 and Ta0.14 single crystals. **b**, Extracted in-plane lattice constants for these three single crystals.

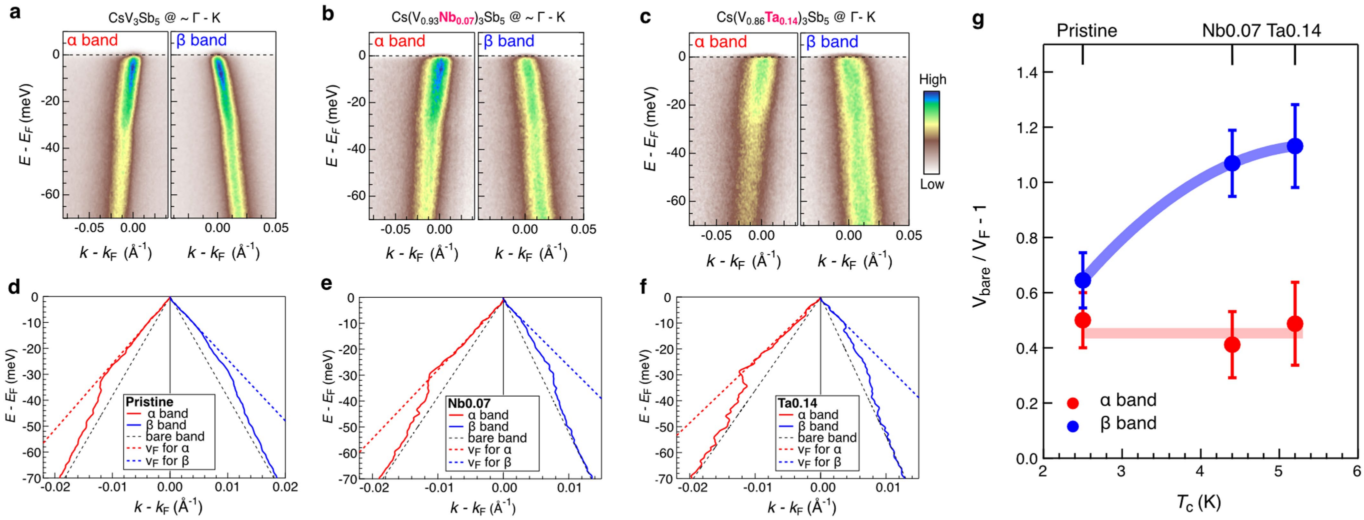

Extended Data Fig. 6 | Spectral evidence of the electron-phonon coupling. **a**–**c**, ARPES intensity plots of the α and β bands nearly along Γ–K direction for the pristine CsV_3Sb_5, Nb0.07 and Ta0.14 samples, respectively. These ARPES data are taken with 7-eV laser at T = 6 K. **d**–**f**, Extracted band dispersions. **a** and **d** are adopted from the ref. 38, in which the T_c of the measured CsV_3Sb_5 is approximately 2.5 K. **g**, Ratio between the velocity of the bare band and the Fermi velocity for the pristine, Nb0.07 and Ta0.14 samples, plotted as a function of their T_c.

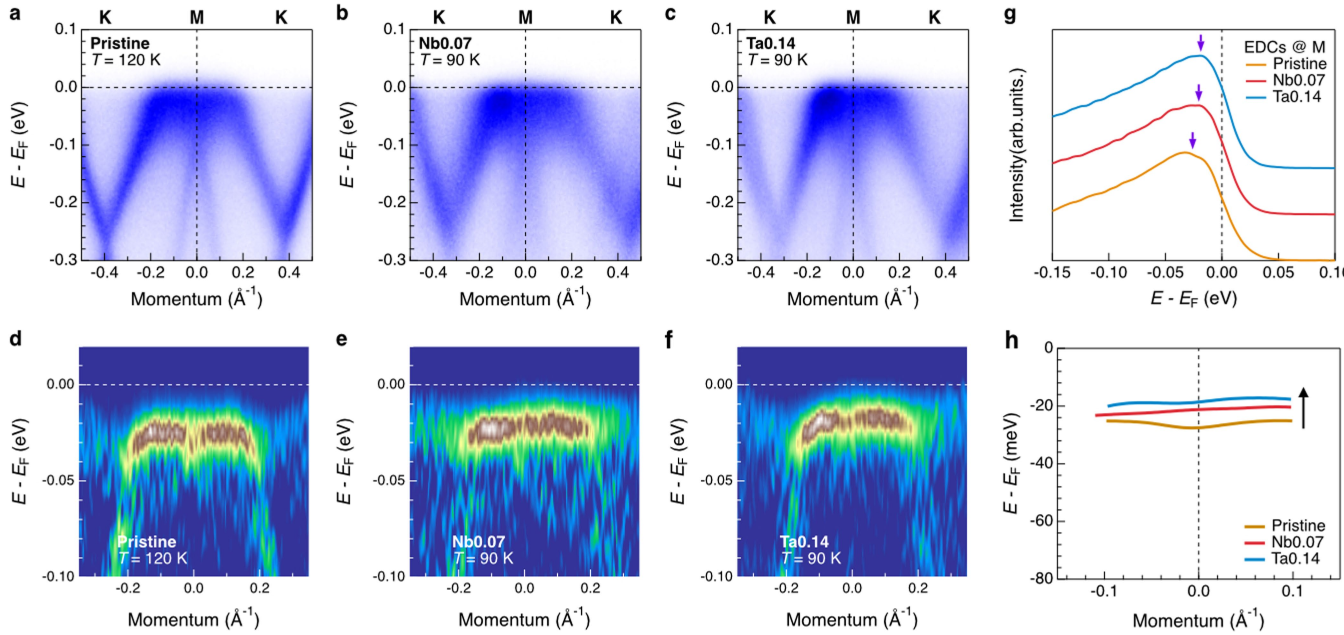

Extended Data Fig. 7 | Comparison of the van Hove singularities. a–**c**, ARPES intensity plots along K-M-K direction for pristine, 7%-Nb and 14%-Ta substituted CsV_3Sb_5, respectively. These ARPES measurements were performed using a photon energy hν = 21.218 eV (He Iα). **d**–**e**, Curvature plots of **a**–**c** near E_F in energy and around M point in momentum. **g**, EDCs extracted at M point. The arrows mark the peak positions of these EDCs. **h**, Band dispersion around M point extracted from the curvature plots.

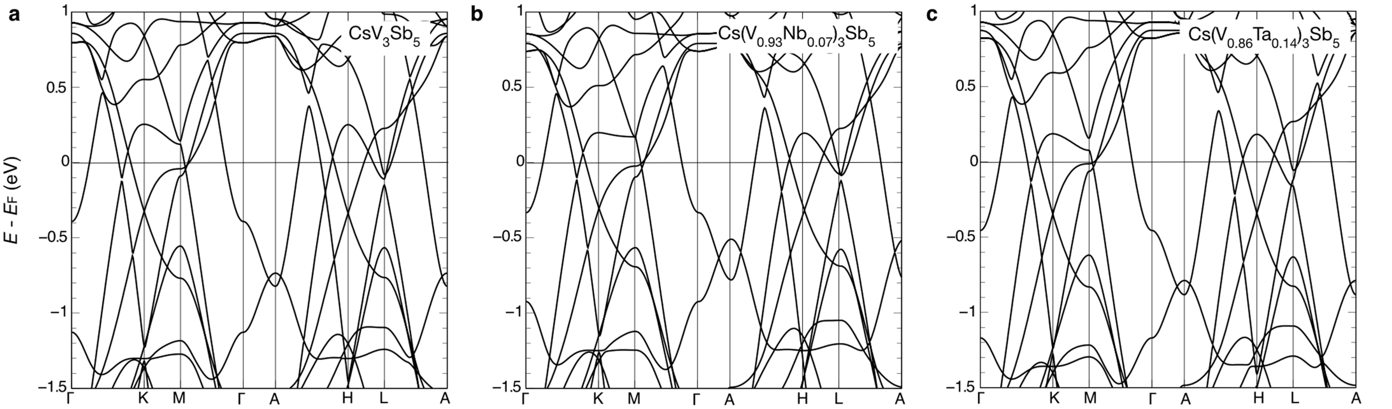

Extended Data Fig. 8 | Calculated band structures for the CsV_3Sb_5, $Cs(V_{0.93}Nb_{0.07})_3Sb_5$ and $Cs(V_{0.86}Ta_{0.14})_3Sb_5$ samples based on density functional theory. The experimentally determined lattice constants are used in the calculation.

Extended Data Table 1 | Statistics of the SC gap for the Ta0.14 samples with $T_c \approx 5.2$ K

Samples	k_F along with	k_F numbers	$\bar{\Delta}$ (meV)	Average deviation (meV)	Δ_{max}- Δ_{min} (meV)	$2\bar{\Delta}/k_B T_c$
Ta0.14 #1	α FS	23	0.78	0.03	0.16	3.48
Ta0.14 #2	β FS	10	0.76	0.02	0.08	3.40
	δ FS	16	0.77	0.04	0.16	3.44
Ta0.14 #3	β FS (around M)	34	0.78	0.03	0.21	3.48
	Average		0.77	-	-	3.44

The SC gap amplitudes on different FSs of different samples are highly consistent and averaged at 0.77 meV, giving $2\Delta/k_B T_c$ of 3.44.

Extended Data Table 2 | Statistics of the SC gap for the Nb0.07 samples with $T_c \approx 4.4$ K

Samples	k_F along with	k_F numbers	$\bar{\Delta}$ (meV)	Average deviation (meV)	Δ_{max}- Δ_{min} (meV)	$2\bar{\Delta}/k_B T_c$
Nb0.07 #1	α FS	25	0.55	0.03	0.17	2.87
Nb0.07 #2	β FS	18	0.48	0.03	0.16	2.52
	δ FS	15	0.51	0.02	0.08	2.67
Nb0.07 #3	β FS (around M)	17	0.52	0.02	0.10	2.75
Nb0.07 #4	β FS	7	0.59	0.02	0.10	3.12
	δ FS	7	0.58	0.03	0.11	3.04
	Average		0.54	-	-	2.83

The SC gap amplitudes on different FSs of different samples are comparable and averaged at 0.54 meV, giving a ratio $2\Delta/k_B T_c$ of 2.83.